Yuanfan Hu ✉
Yongguo Zhu
Xing Yang
Yangfan Tong
Yezhi Teng
Tian Zeng

https://doi.org/10.21278/TOF.501072324
ISSN 1333-1124
eISSN 1849-1391

MODELLING AND PREDICTION OF RIVETING SURFACE DEFORMATION OF AIRCRAFT THIN-WALLED PARTS BASED ON THE SPRING DAMPING METHOD

Summary

Currently, deformation modelling of a riveted assembly of aircraft thin-walled parts typically assumes that the riveted surfaces of thin-walled parts are smooth. However, in engineering practice, the riveted surfaces of thin-walled parts are not smooth. Therefore, in this study, the relationships among the pressing riveting force, the fractal characteristics of the riveting surface, and the riveting deformation are precisely quantified and a new modelling method for predicting the deformation of the riveted assembly of thin-walled components is proposed based on the spring damping method. The method enhances the prediction accuracy of the riveting deformation of aircraft thin-walled components. Through the analysis of the riveted assembly of thin-walled components, the pressing riveting force of the standard pier head is obtained. By examining the microscopic features of the riveting surface, a fractal model capable of capturing the surface complexity at the microscopic scale is established, revealing the geometric and topological properties of the surface. The structural function method is employed to derive the fractal parameters of the equivalent riveting surface topography that characterise the surface roughness. A micro-asperity contact model considering the interactions between micro-asperities is established to simulate the actual contact conditions. By extending the size distribution function of the micro-asperity contact area, a normal contact stiffness and damping model describing the mechanical response of the surface under normal loading is established, incorporating the elastic and dissipative properties of the contact interface. Spring elements representing normal contact stiffness and damping are arranged on the riveting surface to establish a simulation model for the riveted assembly of thin-walled components based on the spring damping method. Simulation and experimental results indicate that, compared with the smooth surface model, the spring damping method model reduces the two indicators of overall relative error by 16% each, and the local relative error of each measuring point by over 8%, thus significantly improving the prediction accuracy. This study integrates the fractal contact theory with the spring damping equivalent method to quantify the influence mechanism of the microscopic topography of the riveting surface on macroscopic deformation, breaking through the limitations of the traditional smooth surface assumption.

Key words: *Thin-walled parts; Riveting; Fractal contact; Spring damping; Finite element*

1. Introduction

Thin-walled parts, such as skins and stringers, are widely used in aircraft structures due to their lightweight and facile formability [1]. Riveting is the main connection form of aircraft thin-walled parts assembly because of its advantages of simplicity of the process, and stable and reliable connection quality [2, 3]. Thin-walled parts of aircraft are susceptible to deformation due to the force applied during riveting, as well as other factors during the assembly process. This deformation can have an impact on the overall accuracy of the aircraft assembly.

In the realm of aircraft construction, the deformation of thin-walled components during the rivet assembly process has garnered substantial attention from the academic community. Numerous scholars have conducted extensive research to delve into the intricate critical manufacturing stage. Theoretical analysis, experimental research, and finite element simulation are commonplace research methods that are utilised. In terms of theoretical analysis, by analysing the stress conditions of a thick-walled cylinder, a calculation model of the pressing riveting force of uneven deformation of the rivet header was established in [4]. Based on the non-uniform distribution of pressure along the thickness direction, an equivalent mechanical model of the riveting process and the relationship between the radial pressure and radial displacement of the rivet hole were established in [5]. The following study used the finite element simulation methods, using a two-dimensional axisymmetric finite element model with an adaptive meshing scheme [6]. To reduce the computational costs and to better describe the deformation of the rivet head, the complex elastic-plastic deformation is replaced by the elastic deformation caused by the local rivet-equivalent element [7]. A hierarchical mapping model was established via the hierarchical mapping method of the local displacement field, thus addressing the issue of the long simulation cycle for predicting the riveting deformation of panels during the aircraft assembly [8]. The deformation of the riveted assembly of thin-walled parts was analysed through a combination of experimental research and finite element simulation [9, 10].

Existing studies on thin-walled part riveting deformation are predominantly macro-scale, assuming ideal smooth surfaces. However, joint interfaces are microscopically rough, resulting in significant discrepancies between theoretical predictions and measured deformations.

To conduct a more realistic and accurate study on the riveted assembly deformation of aircraft thin-walled parts, their surfaces are treated as rough surfaces rather than ideal smooth surfaces. The primary task is to establish the true surface profile of thin-walled parts. At the micro-contact level, the elastic contact model of rough surfaces has received significant attention [11]. In reference [12], an elastoplastic contact model was established based on the principle of volume conservation of asperity plastic deformation. The subsequent study made improvements and obtained a surface contact model that incorporates three deformation states: elastic, elastoplastic, and plastic [13].

All the above models rely on statistical surface topography measurements, which are inherently limited by measurement scale and exhibit instability. In contrast, describing the rough topography of thin-walled parts using fractal functions effectively captures surface complexity and irregularity. In other mechanical components, the tangential contact problem between the piston and the cylinder in the spherical pump was studied using analytical methods and fractal theory [14]. Based on the fractal contact theory, a fractal contact model of the involute spline coupling with surface texture was established [15]. Through numerical studies on rough surfaces, a new method for determining fractal parameters was proposed in [16].

The fractal theory was applied in various studies on mechanical components, such as bolts [17], gears [18], and mechanical seals [19]. To date, no studies have considered rough surfaces in the riveting of aircraft thin-walled parts. By studying the fractal characteristics of mechanical

components, a more realistic contact model is established, which improves the design and analysis level of mechanical structures. This paper takes the deformation of thin-walled parts in the rivet assembly process as the research object. The asperity contact model of the thin-walled parts' riveted surfaces is established by fractal contact theory. Then, the normal contact stiffness and contact damping of the thin-walled parts' riveting surfaces are obtained by expanding the size distribution function of the contact area of the asperity. Then, a modelling method of riveting the assembly of thin-walled parts based on the spring damping method is proposed. Through riveting simulation and experimental comparison analysis, the correctness and effectiveness of the spring damping method model are proved.

2. Creation of a riveted assembly mechanical model for thin-walled parts

The general press riveting process includes a series of operations such as positioning, clamping, drilling, countersinking, riveting, and unclamping. The entire riveting cycle starts with the contact between the riveting die and the rivet and ends when the upset head is fully formed and the die is disengaged. Regarding the deformation of thin-walled components during the riveting process, the drilling operation (*a*) is not included in this analysis. Taking the press riveting of half-round head rivets as an example, the process can be simplified to four stages (*b*, *c*, *d*, and *e*) according to the material flow characteristics. The riveting process and the drilling operation are presented in Fig. 1: (*a*) Drilling thin-walled components. (*b*) Insertion of the rivet into the drilled hole in the thin-walled component, which is placed on the header. Given that the header and the punch are much stiffer than the rivet, and considering that this study is focused on the deformation of the thin-walled component during riveting, the header and the punch are treated as rigid bodies and will be made invisible in the subsequent content. (*c*) The punch touches the head of the rivet, commencing the riveting operation. (*d*) Once the pier head attains the targeted standard size, it brings the entire riveting process to its completion. (*e*) Upon punch unloading, both the rivet and the material surrounding the hole exhibit elastic recovery.

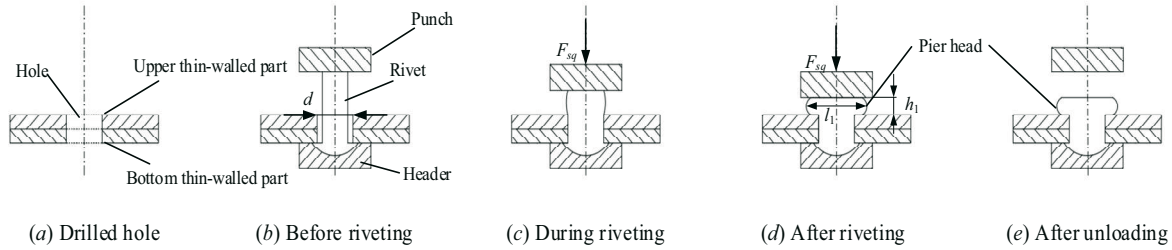

Fig. 1 Rivet assembly process and drilling operation

Upon pier head forming, the pier head is in an instantaneous state of geometric closure. The pier head's lateral surface and other components are no longer in contact due to full material filling, causing lateral constraint forces to dissipate. According to Hill's plastic flow criterion, the free surface stress boundary condition holds when material flow is complete; thus, the pier head's lateral surface can be treated as a free surface, with the radial stress σ_r and circumferential stress σ_θ satisfying the axisymmetric condition, $\sigma_r = \sigma_\theta$.

Under the assumption of quasi-static equilibrium, the side of the header is a free surface, and there is no external force acting on it; therefore, the axial stress on the outside of the header end face is 0, and the relationship between axial stress σ_{1z} and yield stress σ_{1s} can be expressed as [20]:

$$\frac{\sqrt{3}}{2}\left(\arcsin\frac{\sqrt{3}\mu_1\sigma_{1z}}{\sigma_{1s}}-\arcsin\sqrt{3}\mu_1\right)-\frac{1}{2\mu_1}\ln\frac{-\sigma_{1z}}{\sigma_{1s}}=\frac{l_1/2-x}{h_1}, \tag{1}$$

where σ_{1s} is the yield stress of the rivet, σ_{1z} is the axial stress of the rivet, μ_1 is the friction coefficient of the contact surface between the rivet and the punch, l_1 is the diameter of the rivet pier head, h_1 is the height of the pier head, and x is the radial position coordinate of the pier head.

According to the von Mises yield condition, the contact end face of the rivet and the punch meets the following:

$$\sigma_{1z} = -\frac{\sigma_{1s}}{\sqrt{3}h_1^2}r^2 - \frac{\sigma_{1s}}{h_1}\sqrt{h_1^2 - x^2} \tag{2}$$

Integrating Eq. (1) at $x = h_1 \sim l_1$ and Eq. (2) at $x = 0 \sim h_1$, and summing the results, the calculation equation of the pressing riveting force is expressed as follows:

$$F_{sq} = -\frac{\pi h_1^2 \sigma_{1s}}{2\mu_1^2}\left(\frac{13+\sqrt{3}}{3}\mu_1^2 - \ln\frac{1+\sqrt{1-3\mu_1^2}}{\sqrt{3}\mu_1} + 2\sqrt{1-3\mu_1^2} - \sqrt{3}\mu_1 + \frac{1}{\sqrt{3}\mu_1} + \frac{2-\sqrt{3}}{\sqrt{3}}\right) + \frac{\pi l_1 h_1 \sigma_{1s}}{2\mu_1}\left(1-\sqrt{1-3\mu_1^2}\right) \tag{3}$$

From Eq. (3), one can see that the value of the pressing riveting force is related to the material properties of the rivet, the friction coefficient of the contact surface, the height of the pier head, and the diameter of the pier head.

According to the standard pier head size requirements expressed as

$$\begin{cases} h_1 = (0.5 \pm 0.1)d \\ l_1 = (1.5 \pm 0.1)d \end{cases}, \tag{4}$$

where d is the diameter of the rivet hole, the pressing riveting force value required to achieve the standard size of the pier head can be obtained by associating Eqs. (3) and (4).

3. Fractal modelling of riveting surfaces of thin-walled parts

The thin-walled parts are connected by rivets. The contact between the thin-walled parts is not the contact between smooth planes, but the peak-to-peak contact between the asperities on the surfaces of the thin-walled parts. The contact situation between the riveting surfaces of the thin-walled parts is shown in Fig. 2.

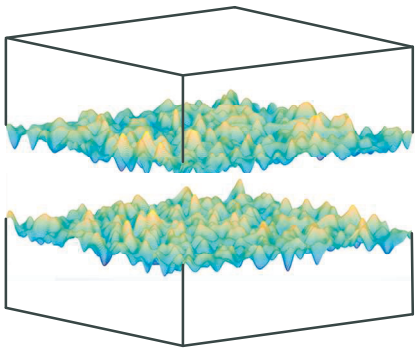

Fig. 2 Riveting surface contact of thin-walled parts

Rough surfaces with fractal characteristics are frequently encountered in practical engineering. This implies that the contour lines of these surfaces mathematically exhibit properties of being everywhere continuous, nowhere differentiable, and self-affine fractals. The

fractal dimension in fractal geometry, characterised by being continuous but non-differentiable within intervals and possessing properties of self-affine fractals, can thus accurately describe and simulate the microtopography of actual rough surfaces. In order to characterise the randomly distributed asperities of different sizes and heights on the surface of thin-walled parts, the W-M fractal function [20] is used to characterise the surface profile of thin-walled parts. The expression is as follows:

$$z(x) = G^{(D-1)} \sum_{n=n_{\min}}^{\infty} \frac{\cos(2\pi\gamma^n s)}{\gamma^{(2-D)n}}, 1 < D < 2, \gamma > 1, \tag{5}$$

where $z(x)$ represents the two-dimensional profile height curve of the rough surface of the thin-walled part, s is the measurement distance, γ is the frequency density in the surface profile, usually $\gamma = 1.5$, n is the frequency index, whose lower limit is determined by $\gamma^{n_{\min}} = 1/L$, and L is the sampling length.

The fractal model of the riveting surface of thin-walled parts is established through the application of the W-M function. The characteristic parameters that describe this model are the fractal dimension D and the surface fractal roughness G. Equation (5) describes a rough surface formed by superimposing a series of cosine-wave asperities with varying sizes. These asperities exhibit isotropic characteristics, and interactions between asperities as well as friction are neglected during the contact. This method can be used to investigate the effects of surface topography on the material surface contact and friction properties.

The contact of the riveting surfaces of the two thin-walled parts are equivalent to the contact between a rough thin-walled part surface and an ideal smooth thin-walled part surface. The equivalent contact of the two thin-walled parts is shown in Fig. 3, the upper surface is the equivalent rough surface of thin-walled parts, and the lower surface is the ideal smooth surface of thin-walled parts. The minimum contact area of the asperity is a_s, the maximum contact area of the asperity is a_l, and the arbitrary contact area of the asperity is a.

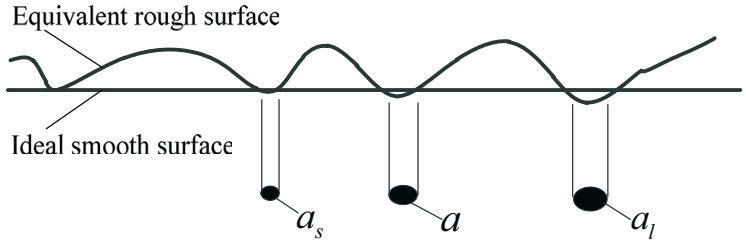

Fig. 3 Schematic diagram of the equivalent contact of the two thin-walled parts

Based on the equivalent elastic modulus in the Hertz contact theory, the relationship between the elastic modulus E of the surface of an equivalent rough thin-walled part and the elastic moduli of the upper and lower thin-walled parts (denoted as E_1 and E_2, respectively) is as follows:

$$\frac{1}{E} = \frac{1-v_1^2}{E_1} + \frac{1-v_2^2}{E_2} \tag{6}$$

In Eq. (6), Poisson's ratio of the upper thin-walled member material is v_1, and Poisson's ratio of the lower thin-walled member material is v_2.

The accurate characterisation of fractal surface profiles hinges on the precise determination of the surface fractal dimension. The structural function method is a methodology used for analysing and solving problems. It decomposes complex problems into multiple

interrelated subproblems and employs different structural functions to describe and analyse the relationships among these subproblems. The structure function method models the surface profile curve as a time series $z(x)$, where $z(x)$ with fractal characteristics ensures that the structure of sampled data obtained from measurements satisfies the following function:

$$S(\xi)=\left\langle\left[z(x+\xi)-z(\xi)\right]^2\right\rangle=\int_{-\infty}^{+\infty}S(\omega)\left(e^{j\omega\xi}-1\right)\mathrm{d}\omega \tag{7}$$

Derive the power spectrum expression of $z(x)$:

$$S(\omega)=\frac{G^{2(D-1)}}{2\ln\gamma}\cdot\frac{1}{\omega^{5-2D}}, \tag{8}$$

where ω is the frequency.

Substituting Eq. (8) into the above equation and integrating yields:

$$S(\xi)=CG^{2(D-1)}\xi(4-2D) \tag{9}$$

Combining Eqs. (7), (8), and (9) yields another expression for the structure function $S(\xi)$:

$$S(\xi)=\left\langle\left[z(x+\xi)-z(\xi)\right]^2\right\rangle=\int_{-\infty}^{\infty}S(\omega)\left(e^{j\omega r}-1\right)\mathrm{d}\omega=C\xi^{4-2D} \tag{10}$$

Its discrete expression is:

$$S(\xi)=\frac{1}{N-\xi}\sum_{\xi=1}^{N-\xi}\left[z(x+\xi)-z(x)\right]^2, \tag{11}$$

where N is the number of sampling points, $\langle\ \rangle$ denotes the spatial average, and ξ represents the data step in the horizontal direction.

Form the above analysis, it follows that determining the two parameters, D and G, of a rough surface profile using the structural function method eliminates the need for spectral analysis of the measured rough surface profile signals and allows them to be directly calculated from Eq. (11).

Therefore, in this paper, the structural function method is used to solve the two fractal parameters, D and G. The structural function method from the reference [22] can be defined as the incremental variance of the profile function of the rough surface of the thin-walled part $H(\xi)$, and its expression is:

$$H(\xi)=\left[z(x+\xi)-z(x)\right]^2=C\xi^{(4-2D_s)}, \tag{12}$$

where C is the correlation coefficient, D_s represents the fractal dimension of the cross-section profile on the rough surface, and the relationship with the fractal dimension D of the rough surface is $D=D_s+1$.

Taking the logarithm on both sides of Eq. (12) simultaneously yields the fractal log-log curve using the structure function method:

$$\log H(\xi)=(4-2D_s)\log\xi+\log C \tag{13}$$

Therefore, $\log H(\xi)$ and $\log \xi$ are linearly related, and the slope of the line formed by $\log H(\xi)$ and $\log \xi$ is b, and the intercept is c. By combining Eq. (5) and $D = D_s + 1$, we can obtain that the fractal dimension D can be obtained by calculating the slope of the line, and the fractal roughness G can be obtained by calculating the intercept of the line; then the expression is as follows:

$$\begin{cases} D = 3 - b/2 \\ G = 10^{\frac{c}{2(D-2)}} \end{cases} \tag{14}$$

Since the surface morphology of the two thin-walled parts is different, the structure functions of the rough surfaces of the two thin-walled parts are $H_1(\xi)$ and $H_2(\xi)$, respectively, and the fractal parameters of the equivalent rough thin-walled surface of the riveting surfaces $H_e(\xi)$ of the two thin walled parts can be obtained by the following equation:

$$H_e(\xi) = H_1(\xi) + H_2(\xi) = C_1 G_1^{2(D_1-1)} \xi^{(4-2D_1)} + C_2 G_2^{2(D_2-1)} \xi^{(4-2D_2)} \tag{15}$$

Based on the fractal contact theory, a fractal model of the riveted surface of thin-walled parts is established, which better conforms to the actual contact condition of the riveted surface. Furthermore, the fractal parameters of the equivalent riveted surface topography are acquired through the structure function method. Then, we establish the contact model of micro-asperities on the riveting surface based on the fractal parameters of the equivalent rough thin-walled surface of the riveting surfaces obtained using Eq. (15).

4. Creation of a model of riveted thin-walled parts based on the spring damping method

4.1 A model of micro-asperity contact of the riveting surface

Since the actual contact area of the riveted surfaces of the thin-walled parts is the sum of the contact area of all the asperities on the riveted surfaces, the contact of a single pair of asperities is studied. The asperities on the riveted surfaces of thin-walled parts are regarded as spheres [23], as shown in Fig. 4, which shows a contact diagram of a pair of asperities. When there is no pressing riveting force, the asperity is opposite to the peak of the asperity, and the contact state is shown in Fig. 4(a). When the rivet is subjected to the pressing riveting force F_{sq}, the rivet rod is deformed and the load is applied to the thin-walled parts. At this time, the asperity is subjected to load, and the contact deformation occurs. The contact state is shown in Fig. 4(b); the contact deformation state of the asperities after the pressing riveting force is equivalent to the contact between an asperity and a smooth plane. The equivalent contact state is shown in Fig. 4(c).

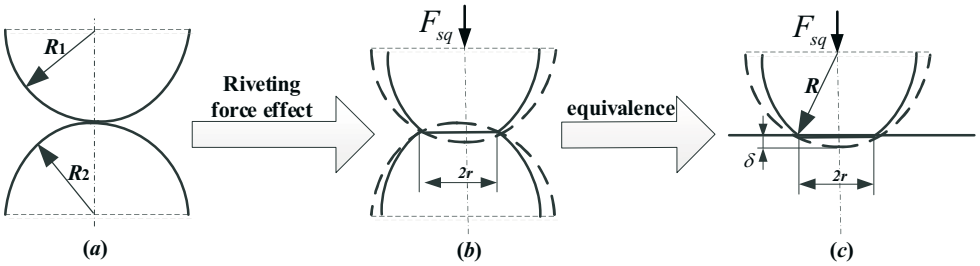

Fig. 4 Schematic diagram of the asperity contact

When subjected to a pressing riveting force, the contact area of any single pair of asperities is $a = \pi r^2$. It can be obtained from the fractal contact theory stating that r is the radius of the contact area of the asperities:

$$r = \left(3F_{sq}R/4E\right)^{1/3} \tag{16}$$

Taking the limit of the derivative of Eq. (5) with respect to x, we obtain the radius of curvature of the equivalent asperity R:

$$R = a^{0.5D}G^{1-D} \tag{17}$$

At the same time, if we evaluate Eq. (5) at $x = 0$ [24], the deformation of the asperity δ is as follows:

$$\delta = G^{(D-1)}a^{(2-D)/2} \tag{18}$$

When a single pair of asperities is in the critical state of elastic and plastic deformation, we can obtain the critical deformation of the asperity δ_c by combining Eqs. (5), (12), and (13):

$$\delta_c = \frac{k^2 a^{D/2}\varphi^2}{4G^{D-1}} \tag{19}$$

In the above equation, k is the constant of proportionality, $k = H/\sigma_s$, φ is the coefficient related to the modulus of elasticity E of the bonding surface, and σ_s is the yield strength of the softer material, $\varphi = \sigma_s/E$.

When $\delta = \delta_c$, the critical contact area a_c of the asperity can be expressed as:

$$a_c = \frac{G^2}{\left(k\varphi/2\right)^{2/(D-1)}} \tag{20}$$

According to the Hertz contact theory, when the contact area of the asperities satisfies condition $a > a_c$, a single pair of asperities is in the elastic deformation stage, and the elastic contact load can be expressed as follows:

$$f_e = \frac{4\sqrt{\pi}EG^{(D-1)}}{3}a^{(3-D)/2} \tag{21}$$

When the contact area of the asperities satisfies condition $a < a_c$, we can substitute Eqs. (17) and (18) into Eq. (21); the obtained result shows that the single pair of asperities enters the plastic deformation stage. Then, the plastic contact load can be expressed as follows:

$$f_p = Ya, \tag{22}$$

where Y is the stiffness of the softer material in the two thin-walled parts.

Since the contact of each pair of asperities is regarded as the contact of spheres, the equation for the contact stiffness between spheres in the Hertz theory can be applied directly. Thus, the contact stiffness of any equivalent spherical asperities in contact with a rigid plane is expressed as

$$k_n = \frac{4E}{3} R^{1/2} \delta^{1/2} = \frac{4E\sqrt{a}}{3\sqrt{\pi}} \tag{23}$$

When the thin-walled parts are subjected to pressing riveting force and the asperities deform elastically, the elastic strain energy of a single pair of asperities can be obtained by integrating the elastic contact load over the amount of deformation:

$$w_e = \int_0^{\delta} f_e(e)\,\mathrm{d}\delta \tag{24}$$

When the asperities undergo plastic deformation, the plastic strain energy of a single pair of asperities can be obtained by integrating the plastic contact load over the amount of deformation:

$$w_p = \int_0^{\delta} f_p(e)\,\mathrm{d}\delta \tag{25}$$

In the study [25], it is shown that the size distribution of the contact area of asperities on the surface of thin-walled parts is in accordance with the theory of island area distribution in the ocean. Through the island area distribution theory, one can obtain the number of asperities on the surface of thin-walled parts with the asperity contact area greater than a as follows:

$$N(A > a) = \left(\frac{a_l}{a}\right)^{D/2} \tag{26}$$

According to the Hertz contact theory, the size distribution function $n(a)$ of the contact area of the asperities is expressed as:

$$n(a) = \frac{\mathrm{d}N}{\mathrm{d}a} = \frac{D}{2}\psi^{(2-D)/2}\frac{a_l^{D/2}}{a^{(D/2+1)}}, \tag{27}$$

where ψ is the domain extension factor related to the distribution of contact area of asperity, and it is also a function related to the fractal dimension D. It is expressed as:

$$\psi^{(2-D)/2} - \left(1+\psi^{-D/2}\right)^{-(2-D)/D} = \frac{2-D}{D} \tag{28}$$

The real contact area formed by the deformation of all asperities on the riveted surface is A_r, which should include the sum of the contact area of the asperities undergoing two stages of elastic deformation and plastic deformation:

$$A_r = \int_0^{a_c} n(a)a\,\mathrm{d}a + \int_{a_c}^{a_l} n(a)a\,\mathrm{d}a = \frac{Da_l}{2-D} \tag{29}$$

4.2 A model of normal contact stiffness and normal contact damping of the riveting surfaces

The normal contact stiffness and normal contact damping of the riveted surfaces of the thin-walled part are the sum of the contact stiffness and contact damping of all the asperities on the riveted surfaces. Therefore, the normal contact stiffness K_n of the riveted surfaces of thin-walled parts can be obtained by using the size distribution function $n(a)$ to expand the normal stiffness k_n of the asperities:

$$K_n = \int_{a_c}^{a_l} k_n n(a)\,\mathrm{d}a = \frac{4ED}{3\sqrt{\pi}(1-D)}\left(a_l^{1/2} - a_l^{D/2} a_c^{(1-D)/2}\right) \tag{30}$$

In order to solve the total strain energy of the riveted surfaces of thin-walled parts, it is necessary to extend the elastic-plastic strain energy of a single pair of asperities to the whole riveting surface through the size distribution function $n(a)$. The total elastic strain energy of the riveted surfaces is the integral of the elastic strain energy of the single asperity from the critical contact area a_c to the maximum contact area a_l:

$$W_e = w_e \int_{a_c}^{a_l} n(a)\,\mathrm{d}a \tag{31}$$

The total plastic strain energy at the riveting surfaces is the integral of the plastic strain energy of the single asperity from the minimum contact area a_s to the critical contact area a_c:

$$W_p = w_p \int_{0}^{a_c} n(a)\,\mathrm{d}a \tag{32}$$

The damping loss factor η of the riveting surfaces can be obtained from the total elastic and plastic strain energies:

$$\eta = \frac{W_p}{W_e} \tag{33}$$

Therefore, the normal contact damping value C_n of the riveted surfaces of thin-walled parts is:

$$C_n = \frac{\eta C_c}{2} = \eta\sqrt{MK_n}, \tag{34}$$

where M is the mass of the thin-walled parts, C_c is the critical damping coefficient, and $C_c = 2\sqrt{MK_n}$.

4.3 Creation of the riveting model of thin-walled parts based on the spring damping method

In order to equalise the normal contact stiffness and normal contact damping of the actual thin-walled riveting surfaces, shown in Fig. 5, an equivalent model using spring elements on the smooth thin-walled riveting surfaces is proposed.

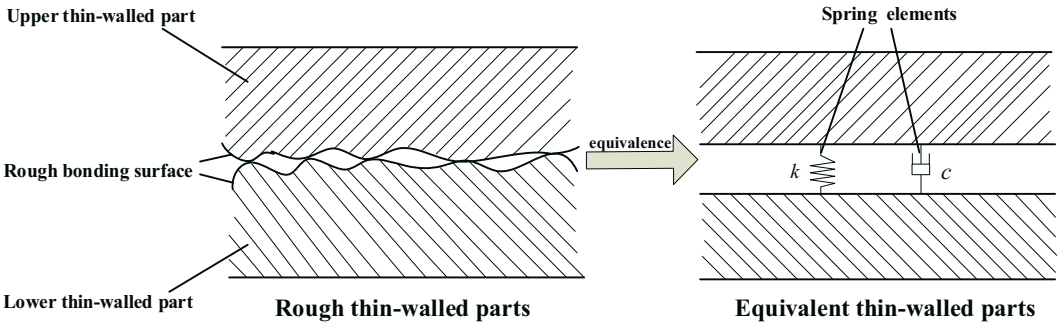

Fig. 5 Equivalent model of spring elements

During the rivet assembly process, the contact stress area between the two thin-walled parts is mainly around the rivet hole, and the area of the contact stress area tends to a fixed value after the riveting is completed. When it is in this range, the contact stress value changes

greatly. When it is beyond this range, the contact stress value changes little. Therefore, the spring elements are set on the circumference of the area. In that case, the normal contact stiffness and normal contact damping values of the riveting surfaces of the thin-walled parts are divided among each spring element. According to Eqs. (30) and (34), the contact stiffness k_s and contact damping c_s of each spring element are obtained as:

$$\begin{cases} k_s = K_n / n \\ c_s = C_n / n \end{cases} \tag{35}$$

5. Application cases

In this section, finite element simulations of the rivet assembly process based on the smooth surface model and the spring damping method model, as well as actual riveting process experiments, are carried out. The accuracy of the spring damping method model is verified by analysing the deformation of thin-walled components after riveting and by comparing the evaluation indices of the experiments.

During the assembly of aircraft thin-walled components, requirements for profile accuracy are imposed, including surface smoothness, waviness, and outer edge profile values. Given that aircraft thin-walled components exhibit low out-of-plane bending stiffness, and fixture constraints fully restrain in-plane displacements (x, y directions) as well as rigid-body motions, the deformation induced by riveting assembly loads is primarily manifested as a z-direction displacement [7, 26]. In the aerospace manufacturing practice, the z-direction displacement is widely adopted as a direct indicator for evaluating the assembly deformation degree of thin-walled components (SAE AS9102, NAS 979). Thus, following the common practice in engineering applications, this paper employs the z-direction displacement to characterise the deformation of components [27, 28].

5.1 Finite element modelling

5.1.1 The smooth surface model modelling

The simulation of riveting thin-walled parts was completed in the explicit dynamics' module of ANSYS Workbench software. The specific operations of the simulation are shown as follows:

First, a three-dimensional model is established in the CATIA software, and then the model is imported into the ANSYS Workbench software, as shown in Fig. 6. Geometric dimensions of the model are shown in Table 1. The material of the rivet is 2A10 aluminium alloy, and the materials of the upper and lower thin-walled parts are 7075 aluminium alloy. The specific material parameters of the thin-walled parts and the rivet are shown in Table 2. The stiffness of the header and punch is much greater than that of other components. Therefore, they are set as rigid bodies. The contact relationship between all components is set as frictional contact, and the coefficient of friction is set to 0.15. The value of the riveting force F_{sq}, determined by simultaneously solving Eqs. (3) and (4), is 36,000 N. To accurately describe the deformation of rough thin-walled parts, all components except the rigid bodies are meshed using C3D8R elements, which in total consist of 42867 elements and 342936 nodes. The riveting process of a single rivet is divided into three analysis steps. In the loading step, the riveting die forms the rivet through pressing; in the holding step, the riveting die remains stationary; in the unloading step, the riveting die retracts. Each analysis step lasts for 0.1 second. The initial state of the cross-sectional mesh of the finite element model is shown in Fig. 7. Fixed constraints are applied to the ends of the thin-walled parts, and the header is also fixed with constraints; riveting

is performed in a consistent front-to-back sequence, activated by punch movement. To ensure the accuracy of the experiment, the same computer configuration was adopted in this paper. The computer is configured with an Intel (R) Core (TM) i5 6500 CPU, 3.2 GHz, and has a memory of 32 GB.

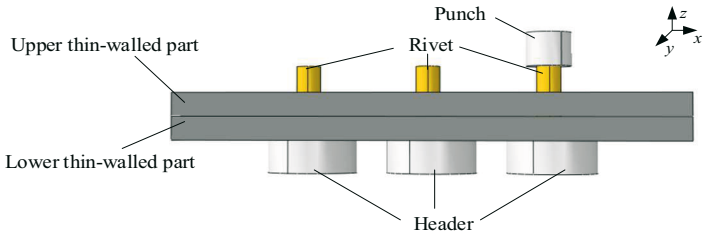

Fig. 6 Finite element model

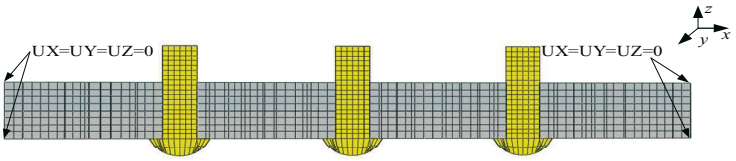

Fig. 7 3D Model of cross-sectional mesh

Table 1 Geometric parameters used in the finite element model

Parameter	Value (mm)
Rivet length h_0	10
Rivet diameter d_0	5
Hole diameter D_0	5.08
Dimensions of thin-walled components	120×60×2

Table 2 Material parameters

Parts	Material	Elastic modulus (GPa)	Density (kg/mm^3)	Poisson's ratio (-)	Yield strength (MPa)
Thin-walled part	7075	71.2	2.77e-6	0.33	503
Rivet	2A10	72.6	2.80e-6	0.33	256

5.1.2 The spring damping method model modelling

This section deals with the creation of the spring damping method model, explains the parameter settings, and elaborates on the specific rationales.

In the ANSYS Workbench software, the COMBIN14 spring elements are utilised to model the riveted interfaces of thin-walled components. By using Eqs. (6) and (14), the equivalent fractal dimension D of the riveting surfaces of the thin-walled part is calculated as 1.4245, and the equivalent fractal roughness G is 1.36×10^{-5}. By substituting Eqs. (30) and (34) into Eq. (35), the normal contact stiffness k_s of the riveting surfaces is calculated to be 2.484×10^{6} N/mm and the normal contact damping c_s is 41.0649 N·s/mm. The computed normal contact stiffness and normal contact damping are respectively assigned as parameters to the spring elements. The explicit dynamics module of ANSYS Workbench software is employed for simulation analysis. The spring damping method model and the smooth surface model are set with identical material properties, meshing parameters, and boundary conditions. The pressing riveting force in the simulation is also specified as 36000 N.

Based on the analysis of the contact stress results of the riveted thin-walled components [29, 30], it is ascertained that the range of stress variation on the thin-walled parts is within the scope of $l \leq 6R_0$ in the vicinity of the rivet hole. When $l > 6R_0$, the stress variation is minimal. Consequently, the spring elements are positioned on the circumference surrounding the rivet hole with $l = 6R_0$. An increase in the quantity of spring elements will enhance the solution accuracy to a certain degree; however, an excessive number of elements will result in an unduly prolonged simulation duration.

To verify the accuracy of using four spring elements for the circumference of a single rivet hole, different experiments were conducted on the element of a single rivet circumference. Figures 8 and 9 show the distribution of z-direction displacement and stress results for different numbers of spring elements, respectively, and Table 3 shows the comparison of the computation times.

As shown in Figs. 8 and 9, significant differences in the distribution of z-direction displacement and stress exist between the 3-element and 4-element spring damping models, indicating less accurate results for the former. Although the 4-element and 5-element models exhibit negligible differences in the distribution of z-direction displacement and stress, the computation time increases excessively for the 5-element model. Fewer spring elements lead to less accurate results, while more elements prolong computation time. The 4-element spring damping model provides an optimal balance between accuracy and efficiency.

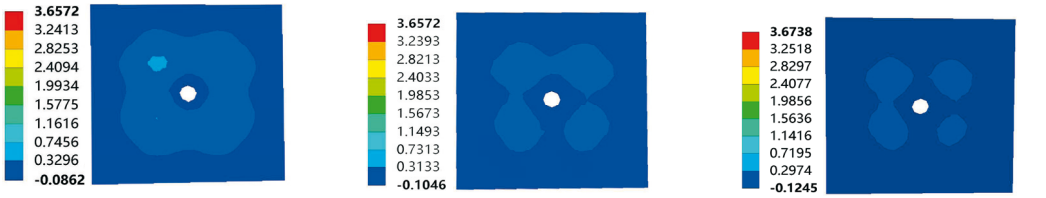

(*a*) Displacement of the five spring-damping element model

(*b*) Displacement of the four spring-damping element model

(*c*) Displacement of the three spring-damping element model

Fig. 8 Distribution of z-direction displacement (mm)

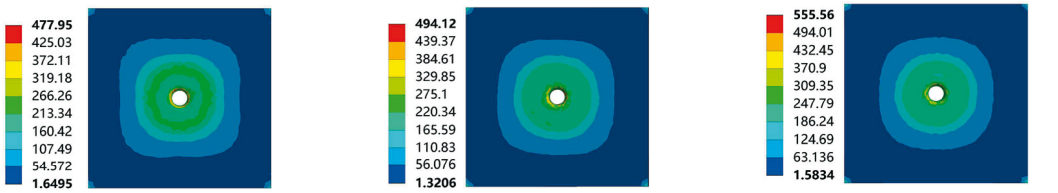

(*a*) Stress of the five spring-damping element model

(*b*) Stress of the four spring-damping element model

(*c*) Stress of the three spring-damping element model

Fig. 9 Distribution of von Mises stress (MPa)

Table 3 Comparison of computation times

Number of spring elements	Computation time (min)
3	9.3
4	10.5
5	15.8

Based on the simulation results, the circumferential arrangement of four COMBIN14 spring elements uniformly distributed around each rivet hole meets the accuracy requirements of this study. Therefore, this layout scheme of spring elements for individual rivet holes on the riveted surface of the thin-walled component is shown in Fig. 10. Four spring elements are

evenly distributed on the circumference of $l = 6R_0$ around the rivet hole. At each rivet hole of the thin-walled component, four COMBIN14 spring elements are uniformly arranged on the circumference with a radius of $l = 6R_0$ (distribution shown in Fig. 10), with a total of 12 spring elements set for all rivet holes.

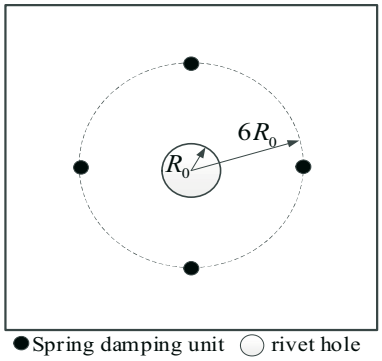

Fig. 10 Arrangement of spring elements

5.2 Simulation results

Finite element simulated z-direction displacement contours are shown in Fig. 11, and von Mises stress contours in Fig. 12. Since both ends of the thin-walled component are fixed during the rivet assembly process, z-direction displacements at these regions are minimal in both models. Characteristic distributions of displacement and stress contours show consistent patterns between the two models.

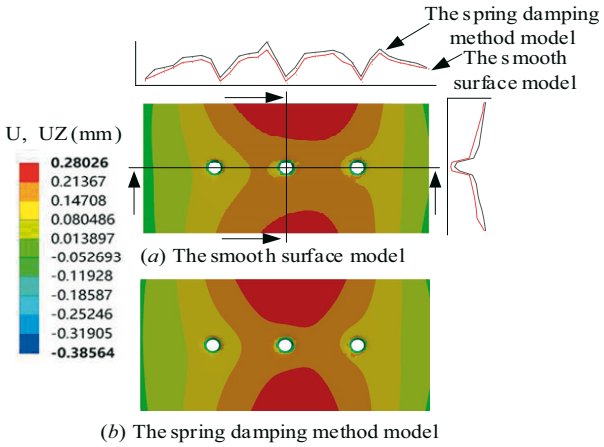

Fig. 11 The z-direction displacement contours

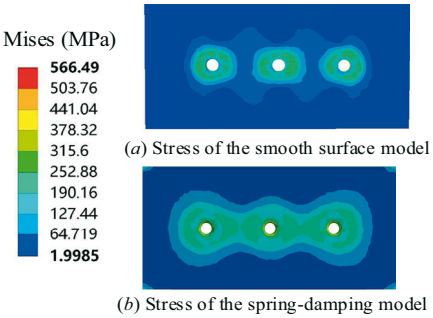

Fig. 12 The von Mises stress contours

5.3 Experimental verification

The riveting is carried out by the automatic riveting machine shown in Fig. 13. In the experiment, the pressing riveting force F_{sq} applied by the punch is 36000 N; it is set through the control screen. Figure 14 shows the riveted structural parts.

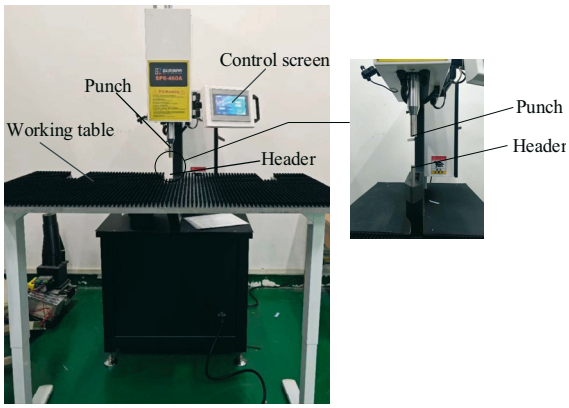

Fig. 13 Riveting experiment of thin-walled parts

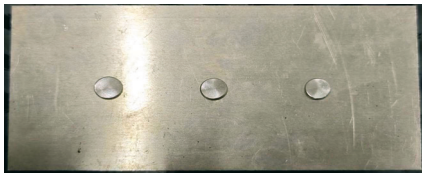

Fig. 14 Riveting structural parts

Topographic data of the thin-walled part surface were acquired using a coordinate measuring machine. Given the large data volume, only partial data are listed in Table 4 to clearly present the key information.

Table 4 Riveting surface point cloud data of thin-walled parts

x (mm)	y (mm)	z (mm)	x (mm)	y (mm)	z (mm)
0	0	-0.0275	0	5	-0.025
0	1	0.0185	0	6	0.0181
0	2	-0.0351	0	7	-0.035
0	3	-0.0354	0	8	-0.0351
0	4	-0.0091	0	9	-0.0092
…	…	…	…	…	…

As shown in Fig. 15, 10 measuring points were uniformly selected on both sides of the rivet hole in the thin-walled part.

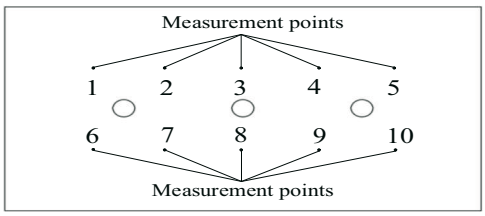

Fig. 15 Distribution of the measurement points

Table 5 and Fig. 16 show the z-direction displacement values of the measurement points in different experiments for the thin-walled part after the rivet assembly process. To achieve

reasonable error quantification, the global results of the smooth surface model have been calibrated to match the z-direction displacements of points 1, 6, and 10 in the actual experiment. On this basis, the z-direction displacement values of each measuring point are found to be roughly consistent with the real experimental results, with local error extremes concentrated at points 3 and 8. Since these measurement points are not located at the fixed ends of the thin-walled part, the z-direction displacement values of each point are non-zero and non-identical.

Table 5 Experimental data and simulation results

Measurement point	Real experiment (mm)	The smooth surface model (mm)	The spring damping method model (mm)
point 1	0.091	0.069	0.089
point 2	0.177	0.152	0.176
point 3	0.242	0.195	0.239
point 4	0.224	0.201	0.218
point 5	0.167	0.138	0.165
point 6	0.089	0.063	0.086
point 7	0.164	0.138	0.159
point 8	0.225	0.172	0.222
point 9	0.217	0.179	0.215
point 10	0.156	0.129	0.154

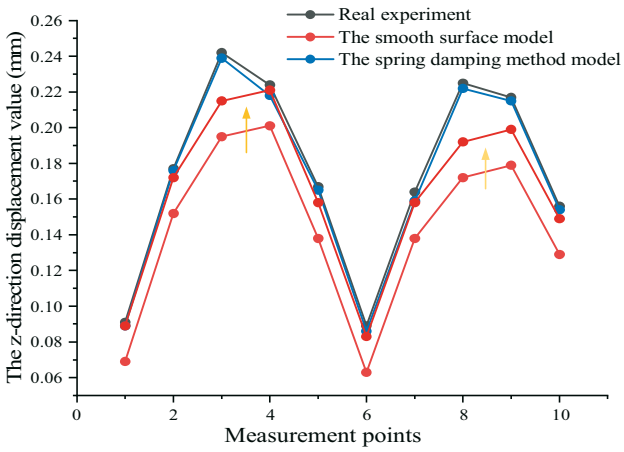

Fig. 16 Comparison of experimental and simulation results

There are requirements for the shape accuracy in aircraft assembly; the evaluation of the overall deformation of thin-walled parts is among them. It can be characterised by the following displacement characteristic values: (1) the maximum value $V_{\max}$ of the z-direction displacement at the measurement points; and (2) the root mean square V_{rms} of the z-direction displacement at the measurement points. The former value, $V_{\max}$, reflects the requirements for the outer contour values of the thin-walled parts after riveting, and the latter, V_{rms}, represents the degree of dispersion of the displacement at the measurement points, which characterizes the smoothness of the shape of the thin-walled parts [7, 26].

The calculation method of V_{rms} is as follows:

$$V_{rms} = \sqrt{\sum_{i=1}^{n} z_i^2 \Big/ n} \tag{36}$$

In the equation, n is the number of measurement points, and z_i is the z-direction displacement at the measurement points.

Table 6 shows the indices obtained from each measuring point in different experiments.

Table 6 Experimental data index

Experiment	Index	
	$V_{\max}$ (mm)	V_{rms} (mm)
Real experiment	0.242	0.1825
The smooth surface model	0.201	0.1505
The spring damping method model	0.239	0.1796

The relative error C can be obtained by the following equation:

$$C = \left| \frac{(A-B)}{B} \times 100\% \right| \tag{37}$$

In the above equation, A denotes the index value and z-direction displacement value of a single measuring point from the smooth surface model or the spring damping method model, and B denotes those from the actual experiment.

According to Table 5, the displacement value of the point of the thin-walled part measured in the experiment is higher than that obtained from the finite element simulation; this is due to the influence of the machining error of the riveting aperture of the thin-walled part and the artificial factors in the experiment. The spring damping method model exhibits closer proximity to the experimental results in the displacement values compared with the smooth surface model.

From Table 6 and Eq. (37), one can see that, compared with the real experiment, the relative errors of index $V_{\max}$ of the smooth surface model and the spring damping method model are 17% and 1%, respectively; the errors of index V_{rms} are also 17% and 1%, respectively.

The local relative errors of individual measuring points calculated using Eq. (37) are shown in Table 7.

Table 7 Local relative error

Measurement point	The smooth surface model	The spring damping method model
point 1	24%	2%
point 2	14%	1%
point 3	19%	1%
point 4	10%	2%
point 5	17%	1%
point 6	29%	3%
point 7	15%	3%
point 8	23%	1%
point 9	17%	1%
point 10	17%	1%

Table 7 shows that, among all measuring points, the maximum local relative error for the smooth surface model is 29% and the minimum is 10%, with the local relative errors of points 1, 6, and 10 being 24%, 29%, and 17%, respectively; for the spring damping model, the

maximum local relative error is 3% and the minimum is 1%, with those of points 1, 6, and 10 being 2%, 3%, and 1%, respectively.

Compared with the smooth surface model, the overall relative errors of the two indicators, $V_{\max}$ and V_{rms}, in the spring damping method model are both reduced by 16%, and the local relative errors of individual measuring points are reduced by 8% or more.

6. Conclusion

In order to improve the accuracy of deformation prediction for the rivet assembly process of aircraft thin-walled parts that are not smooth, an asperity contact model for the thin-walled parts' riveting surfaces based on the fractal contact theory is presented in this paper. Then, through the size distribution function of the asperity contact area, the normal contact stiffness and contact damping of the thin-walled parts' riveting surfaces are obtained, and a riveting assembly modelling method for thin-walled parts based on the spring damping method is proposed. Through riveting simulation and comparative analysis of experiments, the accuracy and effectiveness of the spring damping method model are verified. The following conclusions can be drawn from this study:

(1) A fractal model of thin-walled part riveting surfaces is developed, matching actual contact conditions. Equivalent surface morphology characteristic parameters are extracted using the structure function method.

(2) An asperity contact model is established for the riveting surfaces of thin-walled parts. By expanding the size distribution function of the asperity contact area, the normal contact stiffness and normal contact damping of the riveting surfaces of thin-walled parts are obtained, and a riveting assembly model of thin-walled parts based on the spring damping method is proposed.

(3) From the comparative analysis of the smooth surface model, the spring damping method model, and the actual experimental results, it is evident that the computational results of the spring damping method model exhibit a higher degree of agreement with the actual experimental data. Specifically, compared with the smooth surface model, the two indicators representing the overall relative error are both reduced by 16%, and the local relative errors at all measurement points are reduced by over 8%. This study demonstrates that the riveting assembly modelling method based on the spring damping method can effectively improve the prediction accuracy of the riveting deformation of thin-walled components, thus providing a reliable model for the precise analysis and optimisation of the rivet assembly process of thin-walled components.

Acknowledgments

This study was financially supported by the National Natural Science Foundation of China [52465060]; the Aeronautical Science Foundation [2024M050056002]; and the Key Research and Development Plan Project of Jiangxi Province [20243BBG71004].

REFERENCES

[1] Bałon, P.; Rejman, E.; Świątoniowski, A.; Szostak, J. Thin-walled integral constructions in aircraft industry, Procedia Manufacturing, Vol. 47, (2020), pp. 498-504. https://doi.org/10.1016/j.promfg.2020.04.153

[2] M, Biao.; W, Zhu. Accurate positioning of a drilling and riveting cell for aircraft assembly, Robotics and Computer-Integrated Manufacturing, Vol. 69, (2021), pp. 102-112. https://doi.org/10.1016/j.rcim.2020.102112

[3] Šedek, J.; Růžek, R. Magna-Lok rivet joint and the stiffness-equivalent FE model, Aircraft engineering and aerospace technology, Vol. 91, No. 6 (2019), pp. 834-842. https://doi.org/10.1108/AEAT-07-2018-0188

[4] Z, Chang.; Z, Wang.; B, Wang.; G, Kang.; Q, Luo. Compression riveting force modelling based on uneven deformation of header, Journal of Aeronautics, Vol. 37, No. 7 (2016), pp. 2312-2320 (in Chinese). https://doi.org/10.7527/S1000-6893.2016.0043

[5] B, Zheng.; H, Yu.; X, Lai. Assembly deformation prediction of riveted panels by using equivalent mechanical model of riveting process, The International Journal of Advanced Manufacturing Technology, Vol. 92, (2017), pp. 5-8. https://doi.org/10.1007/s00170-017-0262-9

[6] Zanatta, C.; Villani, E.; Mello, J. Riveting process simulation to predict induced deformations in aeronautical structures, The International Journal of Advanced Manufacturing Technology, Vol. 120, (2022), pp. 11-12. https://doi.org/10.1007/S00170-022-09247-4

[7] D, Yang.; W, Qu.; Y, Ke. Local-global method to predict distortion of aircraft panel caused in automated riveting process, Assembly Automation, Vol. 39, No. 5(2019), pp. 973-985. https://doi.org/10.1108/AA-06-2018-079

[8] Q, Xu.; M, Wang.; W, Chen.; D, Liu. A local displacement field hierarchical mapping method for wall plate deformation prediction, China Mechanical Engineering, Vol. 30, No. 23(2019), pp. 2870-2876+2883 (in Chinese). https://doi.org/10.3969/j.issn.1004-132X.2019.23.014

[9] M, Pan.; W, Tang.; Y, Xing. The deformation analysis, prediction, and experiment verification for thin-wall part assembly based on the fractal theory model with WNNM, The International Journal of Advanced Manufacturing Technology, Vol. 92, (2017), pp. 9-12. https://doi.org/10.1007/s00170-017-0497-5

[10] M, Pan.; W, Tang.; Y, Xing.; J, Ni. The numerical simulation analysis for deformation deviation and experimental verification for an antenna thin-wall parts considering riveting assembly with finite element method, Journal of Central South University, Vol. 25, No. 1 (2018), pp. 60-77. https://doi.org/10.1007/s11771-018-3717-8

[11] Greenwood, J A.; Williamson, J B P. Contact of nominally flat surfaces, Proceedings of the Royal Society of London Series A, Vol.295, (1966), pp. 300-319. https://doi.org/10.1098/rspa.1966.0242

[12] Chang, W.; Etsion, I. An elastic-plastic model for the contact of rough surfaces, ASME Journal of tribology, Vol. 109, No. 2 (1987), pp. 257-263. https://doi.org/10.1115/1.3261348

[13] Y, Zhao.; M, David. An asperity microcontact model incorporating the transition from elastic deformation to fully plastic flow, ASME Journal of tribology, Vol. 122, No. 1 (2000), pp. 86-93. https://doi.org/10.1115/1.555332

[14] D, Guan.; L, Jing. Tangential contact analysis of spherical pump based on fractal theory, Tribology International, Vol. 119, (2018), pp. 531-538. https://doi.org/10.1016/j.triboint.2017.11.034

[15] X, Xue.; K, Lin. Fractal theory-based contact analysis of surface microtextured involute spline coupling, Tribology International, Vol. 200, (2024), pp. 110055. https://doi.org/10.1016/j.triboint.2024.110055

[16] F, Shen.; Y, Li. On the size distribution of truncation areas for fractal surfaces, International Journal of Mechanical Sciences, Vol. 237, (2022), pp. 107789. https://doi.org/10.1016/j.ijmecsci.2022.107789

[17] L, Li.; Q, Yun.; J, Wang.; B, Dong.; H, Shi. A contact stiffness model for bonding surfaces with continuous smoothness, Journal of Mechanical Engineering, Vol. 57, No. 7(2021), pp. 117-124. (in Chinese). https://doi.org/10.3901/JME.2021.07.117

[18] L, Zhu.; G, Wang.; W, He.; W, Fan. Analysis of Contact Strength for Nutation Transmission with Conical Movable Teeth by Fractal Theory, Recent patents on mechanical engineering, Vol. 13, No. 2(2020), pp. 141-155. https://doi.org/10.2174/2212797613666200206152545

[19] X, Ni.; J, Sun.; C, Ma.; Y, Zhang. Wear Model of a Mechanical Seal Based on Piecewise Fractal Theory, Fractal and Fractional, Vol. 7, No. 3(2023), pp. 251-251. https://doi.org/10.3390/FRACTALFRACT7030251

[20] Q, Yin.; Q, Wang.; G, Kang.; Y, hu. Research on the Maximum Riveting Force Based on Theory of Compression Instability, Advanced Materials Research, Vol. 24, No. 33 (2013), pp. 716-744. https://doi.org/10.4028/www.scientific.net/AMR.716.744

[21] B, Lv.; K, Han.; Y, Wang.; X, Li. Analysis and Experimental Verification of the Sealing Performance of PEM Fuel Cell Based on Fractal Theory, Fractal and Fractional, Vol. 7, No. 5(2023), pp. 32273-32286. https://doi.org/10.3390/fractalfract7050401

[22] Y, Zhao.; C, Zhao.; P, Wang. A rail corrugation evaluation method using fractal characterization based on structure function method, Wear, Vol. 24, (2022), pp. 506-507. https://doi.org/10.1016/J.WEAR.2022.204454

[23] J, Cao.; Z, Zhang.; W, Yang.; Y, Guo. Non-uniform virtual material modelling on contact interface of assembly structure with bolted joints, Structural Engineering and Mechanics, Vol. 72, No. 5(2019), pp.557-568. https://doi.org/10.12989/SEM.2019.72.5.557

[24] Y, Wang.; X, Zhang.; S H, Wen. Fractal loading model of the joint interface considering strain hardening of materials, Advances in Materials Science and Engineering, Vol. 1442, (2019), pp.1-14. https://doi.org/10.1155/2019/2108162

[25] W, LIU.; J, Yang.; N, Xi.; J, Shen.; L, Li. A study of normal dynamic parameter models of joint interfaces based on fractal theory, Journal of Advanced Mechanical Design, Systems, and Manufacturing, Vol. 9, No. 5(2015), pp. 70-83. https://doi.org/10.1299/jamdsm.2015jamdsm0070

[26] Z, Chang.; Z, Wang.; L, Xie. Prediction of riveting deformation for thin-walled structures using local-global finite element approach. The International Journal of Advanced Manufacturing Technology, Vol. 97, No. 5(2018), pp. 2529-2544. https://doi.org/10.1007/s00170-018-2050-6

[27] D, Zhao.; W, Wang. Dimensional Deviation Estimation for Parts with Free-Form Surfaces. Mathematical Problems in Engineering, Vol. 2018, No. 1(2018), pp. 4390284. https://doi.org/10.1155/2018/4390284

[28] W, XIAO.; Y, YUAN. Study on deformation measurement method based on structured light point clouds. Journal of Northwestern Polytechnical University, Vol. 41, No. 1(2023), pp. 47-55. (in Chinese). https://doi.org/10.1051/jnwpu/20234110047

[29] Z, Silvayeh.; M, Brillinger.; J, Domitner. Deformation behavior of aluminum alloy rivets for aerospace applications. Journal of Materials Research and Technology, Vol. 33, (2024), pp. 3482-3491. https://doi.org/10.1016/j.jmrt.2024.09.259

[30] H, Hong.; H, Tao.; H, Hai. Study on stress characterisation of interference fit riveting based on tapered holes. Journal of Plasticity Engineering, Vol. 32, No. 1(2025), pp. 112-121. (in Chinese). https://doi.org/10.3969/j.issn.1007-2012.2025.01.012

Submitted: 11.10.2024

Accepted: 29.9.2025

Yuanfan Hu*
Yongguo Zhu
Xing Yang
Yangfan Tong
Department of Aeronautical Manufacturing and Mechanical Engineering, Nanchang HangKong University, Nanchang 330063, China

Yezhi Teng
Tian Zeng
AVIC Jiangxi Hong du Aviation Industry Group Company Ltd, Nanchang 330024, China

*Corresponding author:
h18270315975@163.com